Development of new β/α”-Ti-Nb-Zr biocompatible coating with low Young's modulus and high toughness for medical applications

E. Frutos[1], M. Karlík[2,3], J.A. Jiménez[4], H. Langhansová[5], J. Lieskovská[5], T. Polcar[1,6]

[1] Department of Control Engineering, Faculty of Electrical Engineering, Czech Technical University in Prague, Technická 2, Prague 6, Czech Republic.

[2] Department of Materials, Faculty of Nuclear Sciences and Physical Engineering, Czech Technical University in Prague, Trojanova 13, 120 00 Prague 2, Czech Republic.

[3] Charles University, Department of Physics of Materials, Ke Karlovu 5, 121 16 Prague 2, Czech Republic.

[4] Centro Nacional de Investigaciones Metalúrgicas (CENIM-CSIC), Avd. Gregorio del Amo no 8, 28040 Madrid, Spain.

[5] Faculty of Science, University of South Bohemia and Biology Centre AS CR, Branišovská 31, České Budějovice, Czech Republic.

[6] Engineering Materials, University of Southampton, University Road, Southampton SO17 1BJ UK.

Keywords: Biomaterials, Non-toxic β-rich Ti coatings, Martensitic phase transformation, Rietveld XRD quantification, Transmission electron microscopy, Low Young’s Modulus.

Abstract

Ideal biomaterials to fabricate orthopedic implants, especially for load-bearing joint replacements, should include only non-toxic elements with good biocompatibility, high corrosion resistance and surface bioactivity, together with a good combination of mechanical properties. Based on these criteria, a manufacturing approach based on sputtering techniques can be ideal to develop coatings free of toxic elements tailored for advanced applications on pure titanium or titanium alloys used in biomedical applications. In this work, the ternary Ti-Nb-Zr system was used to develop non-toxic β-rich Ti coatings with several complex microstructures by careful control of Nb and Zr concentration and deposition parameters, such as bias voltage. Depending on the alloy chemistry and processing, the coating included variable amounts of α-, α''- and β-phases of Ti with different morphologies and crystallographic texture. Mechanical properties of every coating is largely determined by the micro-structure present, which is directly related to bias voltage used during sputtering process. Thus, hardness values change as a function of the compressive residual stresses magnitude and Young's modulus decreased from 63 GPa, at 0 V, to 47 GPa, at -63 V, being this value close to human bone (~30 GPa). After that, Young's modulus progressively increases to 89 GPa, at -148 V. On the other hand, bioactivity of the coating is practically doubled when compared to Ti6Al4V alloy.

1. Introduction.

Alloys designed for manufacturing medical implants must present a combination of high strength and fatigue resistance as well as low Young's modulus to guarantee a long-term service life under complex cyclic loading experienced during the routine activities [1]. In the case of alloys used in the design of implants subjected to cyclic load-bearing, such as: hip joint, knee and shoulder prosthesis, tensile strength should be ~1000 MPa [2,3] and and Young's modulus should be close to those of natural human bone (20-30 GPa) [4,5], respectively. However, the combination of high yield strength and low elastic modulus required to materials replacing dysfunctional hard tissue are usually contradictory aspects, for most titanium (Ti) alloys used in medical applications, since the elastic modulus of these alloys (~110 GPa) is much higher than that of the bone. This mismatch in the Young's modulus values produces the presence of the stress shielding effect, which occurs due to insufficient loading of the bone adjacent to the implant. Lack of load-bearing capacity can lead to bone atrophy and therefore loosening of the implant. Therefore, it is necessary to find a processing route able to produce Ti alloys with high hardness and low Young's modulus to ensure a good osseointegration between implants and bone tissues, reducing the number of implant failures and therefore the number of revision surgeries [6,7].

As the elastic modulus is dependent on the lattice parameter, alloys with lower packing density should have a lower Young modulus. Based on these criteria, efforts have been paid to develop Ti alloys with body centered cubic (bcc, β-Ti) instead hexagonal close packed (hcp, α-Ti) crystal structure. Therefore, metastable β-Ti alloys free of toxic and allergenic elements such as Al and Ni can reach Young’s modulus values ranging from 55 to 85 GPa [8,9,10] instead of the reported values for the most widely used alloys, in biomedical applications, that fall in the range of 100 to 220 GPa [5]. Nevertheless, such reduction is still high for preventing stress shielding, and so further research is still required.One of the best ways to further reduce Young’s modulus value is through the combination of different phases such as: α, α´ and ω phases, with hexagonal close-packed (hcp) crystal structure, and β and α”, with body centered cubic and orthorhombic crystal structures, respectively. Young’s modulus increases with the presence of α or ω phase because Young’s moduli of these phases are much higher than that of the β. Therefore, it is reasonable to think that the mixture of β and α” phases leads to a comparatively low elastic modulus in comparison with conventional commercial Ti alloys, e.g. Ti6Al4V ELI (Extra low interstitial) [5].

Alloying elements in solid solution can exert significant influences on proportion of phases present and can lead to a strong manipulation of the lattice parameters of α”, β and α-phases. Thus, depending on the amount of β-stabilizers and the presence of neutral elements such as Zr or Sn [11], a higher or lower α phase content can be introduced for enhancing the yield strength or reducing the Young’s modulus [12]. As the modulus of β alloys can be lowered by decreasing the content of β-stabilizing elements, the lowest modulus will be obtained at the composition containing the least amount of β-stabilizing elements able to maintain this single β phase [13]. Alternatively, a suitable processing route can be used for a further reduction in β-stabilizing non-toxic elements and the incorporation of neutral elements for reducing the modulus [14]. In general, high yield strength and low elastic modulus are contradictory aspects. Therefore, the ideal processing route should confer an optimal balance between α”, β and α-phases that ensures the Young’s modulus much closer to that of the bone, and refine the microstructure up to the nano-metric scale dimension. The very large number of β/α, β/α” and α/α” nano-grains interfaces introduced are very effective barriers to dislocation movement and then enhance the alloy strength. However, these processing routes are complex and extremely costly, since they include several thermos-mechanical steps with high plastic deformation.

An additional aspect that have to be considered for designing and manufacturing metastable β-Ti alloys is the formation of stress induced martensite (SIM). When the content of β-stabilizers is insufficient, the stress due to plastic deformation can induce the martensitic transformation $\beta \rightarrow \alpha''$. The presence of such transformation, minimizes the applicability of this alloy in design of metallic implants with high load-bearing transfer because it gives rise to a very low yield stress and a reduced fatigue resistance [15]. Thus, SIM transformation should be reduce as much as possible. One possible route is to reduce the matensitic start temperature, M_s, since the magnitude of the threshold stress for martensitic transformations decreases with increasing M_s temperature. In this sense, it has been shown in recent investigations that Zr is able to reduce the martensitic start temperature below room temperature depending on the concentration of this element and the concentration of β-stabilizers (Nb, Mo and Ta). Thereby, in order to minimizing the risk of mechanical failure and to avoid the problem of "stress shielding", Ti alloys have to be simultaneously optimized at the structural and chemical levels.

All these requirements could be achieved by the development of surface modifications, in form of coatings, composed with non-toxic elements. In this context, sputtering techniques offer multiple possibilities in the *in-situ* design of complex (near) pure β-Ti textured coatings deposited on pure titanium or titanium alloys. Besides, coatings composed by nano-grains will ensure lower surface roughness, higher wettability and better cell responses as compared with coarse-grained alloys. Among all possible coatings consisting of non-toxic elements, β-rich Ti-Nb-Zr are the most promising candidates, since both elements are extremely biocompatible, exhibiting low ionic cytotoxicity *in vitro*, excellent biocompatibility *in vivo*, no evidence of mutagenicity or carcinogenicity, a good resistance to corrosion, and osseo-compatibility similar or exceeding that of Ti [16]. Moreover, as the balance between α", β and α-phases depends on Zr and Nb content and deposition parameters, such as bias voltage, it is possible to adjust mechanical properties, such as Young's modulus, yield strength and fatigue performance to reflect the functional requirements of implants for a selected replacement applications.

Full potential in the above referred area of coating materials is yet to be explored. Consequently, this work is focused on designing and manufacturing ternary Ti-Nb-Zr coatings composed by a mixture of α, α" and β phases with nano-metric size by direct current (DC) magnetron sputtering deposition technique. These coatings will include a Zr content ranging from 8 and 12 wt. % in order to guarantee its capacity as β stabilizer [17]. On the other hand, the presence of α” phase will be also guaranteed if Nb content is between 13 and 39 wt. %, as occur in binary Ti-Nb alloys [13]. Finally, a presence of a fine dispersed α phase will be secured when the sum of Nb and Zr content will be below 42 wt. % threshold. Mechanical properties will be manipulated by change of volume fraction and variations of main texture between α/β and α”/β ratios through a negative bias voltage increase. Moreover, cell bioactivity will be evaluated for the coating showing the most suitable mechanical properties, low Young’s modulus and high hardness, for the implants design with cyclic load-bearing transfer.

2. Experimental procedures

2.1. Materials synthesis

The Ti-Nb-Zr coatings have been deposited on single crystal (100) Si wafers using a balanced magnetron sputtering apparatus (ATC-Orion 8 UHV from AJA INTERNATIONAL Company, Massachusetts, US). Targets (Kurt J. Lesker Company) of Ti (99,99 % purity), Nb (99,99 % purity) and Zr (99,99 % purity) with a diameter (ϕ) of 50.8 mm have been used to deposit the coatings. The DC sources were located at a target-to-substrate distance of ~ 80 mm and were tilted about 30° to the substrate normal, in order to increase the deposition rates. The chamber was pumped down to a base pressure of 1×10^{-5} Pa, while the depositions were carried out with an Ar gas flow of 0.008 Pa*m^3/s and with a deposition pressure of 0.39 Pa. The substrate holder was rotated at 10 rpm during deposition to ensure composition homogeneity on the substrate. The DC power was kept constant at 371 W for Ti, at 34 W for Nb and at 20 W for Zr. The sputtering yield, S (atom/ion), associated with these power were: 0.42, 0.30 and 0.27, respectively. Therefore, sputter rate, Z/t (nm/s) for each target was: 19.8, 2.2 and 1.4 nm/s respectively. Every deposition was carried out for about 2700 s, resulting in a total film thickness of ≈ 600 nm, evidencing that the efficiency of the process is about 1%. The bias voltage on the substrate during deposition was selected to be 0, -63, -98, -125, and – 148 V.

2.2 Structural and microstructural characterization

The microstructure and its evolution as a function of bias voltage have been investigated by grazing incidence X-ray diffraction (GIXRD) and transmission electron microscopy

(TEM). X ray diffraction (XRD) measurements were carried out with a Rigaku Smart Lab diffractometer (Rigaku Corporation, Japan) with parallel beam geometry (Rigaku Corporation, Japan) in grazing incidence condition. A rotating anode type X-ray generator with Cu target operating at 9 kW (45 kV, 200 mA), was used as an X-ray source and a high speed linear detector D/teX ultra250. XRD data were collected with a beam incidence angle of 1° and 2θ scan between 20 and 80° with a step size of 0.02°. The identification of crystalline phases present in the sputtered Ti-Nb-Zr coatings has been performed from XRD patterns using the JCPDS data base and the DIFFRACplus EVA software by Bruker AXS. However, matching the XRD pattern with the JCPDS data base did not allow to unambiguously characterizing the phases present in the coatings due to systematic peak overlap of Ti phase sand the very strong texture exhibited by sputtered Ti alloys. The Rietveld method is more robust and rigorous technique for phase analysis in very complex systems since the full pattern data are fit and refined, and thus multiple reflections for each phase are explicitly included and preferential orientation corrections can be introduced in the quantitative analysis. In this study we have used version 4.2 of the Rietveld analysis program TOPAS (Bruker AXS) for XRD data refinement. Refinement analyses were carried out using space groups and crystallographic information from Pearson's Crystal Structure database for the phases of Ti [18]. The refinement protocol included also the major parameters like background, zero displacement, the scale factors, the peak breadth and the unit cell parameter parameters.

Thin foils for transmission electron microscopy (TEM) observations have been prepared by cleavage of two samples 5 mm × 3 mm, which were glued together to obtain a Si-thin layer-glue-thin layer-Si sandwich. Cross-sectional slices 0.5 mm thick were then cut using a slow speed diamond saw. These slices were polished from one side, glued to a standard 3 mm copper washer, mechanically thinned to 20 μm, dimple polished, and ion-beam milled in Gatan PIPS 691 device. The samples were examined at 200 kV in a JEOL JEM 2200FS microscope equipped with EDS spectrometer Centurion and NanoMegas ASTAR automated crystal orientation mapping system. Field-emission gun microscope was also operated in nano-beam diffraction mode with a beam ~3 nm in diameter and NanoMEGAS DigiSTAR precession unit has been used for automated spot diffraction data acquisition in the frame of 300 by 300 points with step of 2 nm in order to analyze regions of the thin layer 600 nm by 600 nm. The series of spot diffraction patterns acquired with precession angle 0.7° have been automatically processed using ASTAR software with input crystallographic data (space group, lattice parameters, i.e. $a = 2.976\ \dot{A}, c = 4.740\ \dot{A}$, for hexagonal α-phase, $a = 3.046\ \dot{A}, b = 5.016\ \dot{A}\ and\ c = 4.664\ \dot{A}$, for orthorhombic α”-phase, and $a = 3.319\ \dot{A}$, for cubic β-phase) from previous X-ray diffraction phase analysis to obtain nanocrystal phase and orientation maps of the coatings. Finally, 3D optical profiler (Zygo NewView 7200) has been used to measure the curvature that the sputtering coating surface shows due to the presence of residual stresses.

2.3 Mechanical characterization

Mechanical properties have been determined by nano-indentation tests using Nanotest–Vantage equipment from the Micro Materials Company. Nano-indentations have been performed on the top surface of the Ti-Nb-Zr samples with a Berkovich type indenter, using increasing loads from 1 to 10 mN. Loading and unloading times were fixed at 20 and 5 s in order to fix the strain rate at 0.05 and 0.2 s^{-1}, respectively. In all cases, the hold time was fixed at 15 s. Berkovich hardness, H, and Young's reduced modulus, E_R, have been evaluated from the load depth indentation curves using the Oliver and Pharr method [19]. In both cases, hardness and Young's modulus values for a given load correspond to average values from at least 10 measurements.

The measure of the curvature of the silicon wafer before and after deposition is a useful tool to characterize qualitatively residual stresses as a function of the bias voltage, since the type of curvature as well as its radius will change depending on the character of the residual stresses and its magnitude. In this way a concave curvature is indicative of the presence of compressive residual stresses and a convex curvature is indicative of the presence of tensile residual stresses. From this curvature and using Stoney’s equation [20] it is possible calculate residual stresses values:

$$\sigma = \frac{E_s h_s^2}{6(1-\nu_s)h_f}\left(\frac{1}{R} - \frac{1}{R_0}\right), \qquad (1)$$

where E_s (130 GPa) and ν_s (0.28) represent the Young’s and Poisson modulus of the silicon wafer. Substrate and coatings thickness are represented as h_s (450 µm) and h_f (~0.6 µm), respectively. Finally, curvature radius for substrate and substrate plus coating are represented as R_0 (∞) and R, respectively.

2.4 In vitro *biocompatibility assays*

Human osteosarcoma cell line MG-63 (ATCC® CRL-1427™) was acquired from American Type Culture Collection (ATCC). Cells were grown in RPMI medium supplemented with 10 % fetal calf serum, L-glutamine (292 µg/ml), penicillin G (100 U/ml), streptomycin (100 µg/ml; all from Biowest) and 50 µM mercaptoethanol (Sigma). Cells were maintained at 37 ºC in 5 % CO_2 and 95 % air in a humidified incubator and passaged twice a week. For the cell culture experiments, 13 mm diameter glass cover slips were coated by magnetron sputtering technique, following the same procedure as silicon substrate. All samples were routinely sterilized under UV light in a laminar flow hood for 12 h on each side and stored until use.

For the cell adhesion/proliferation assays, MG-63 cells were seeded on uncoated, Ti-, Ti6Al4V- or Ti22Nb10Zr-coated cover slips in triplicates ($6x10^3$ cells/sample)and cultured in 24-well plates in 1 ml of growth medium for 1, 4 and 7 days. After the time indicated, the samples were transferred into new wells containing 500 µl of fresh culture medium. Viable cells were quantified by AlamarBlue® Cell Viability Reagent (Thermo Fisher Scientific), a redox indicator that yields a fluorescent signal in response to metabolic activity of the cells. After 4-hour incubation in 37 °C and 5 % CO_2, fluorescence was measured in Synergy H1 microplate reader (BioTek) upon excitation and emission wavelength 550 nm and 590 nm, respectively. The values from Ti- and alloy-coated samples were normalized to uncoated glass cover slips which means that metabolic activity of the cells on glass (as a function of cell adhesion and proliferation) is set to 100 %. Data are represented as means ± standard error of mean (SEM) from at least two independent experiments. Differences between samples were evaluated using 2-way analysis of variance followed by Bonferroni post-hoc test. P-values < 0.05 were considered significant.

3. Results

3.1. Microstructural characterization

Cross sectional scanning transmission electron microscopy (STEM) micrographs recorded using the high angle annular dark field (HAADF) mode showed that compact and dense microstructures, without defects such as pores and cracks, were obtained independent of the processing conditions. However, as bias voltage used was increased a transition from a columnar to a finer and more equiaxed grain structure was observed, as shown in Fig. 1a and b for coatings deposited at -63 V and -148 V, respectively. In both coatings, the average column diameter estimated from diffraction contrast TEM images ranged from 5 to 10 nm in size. Structural defects, such as vacancies, dislocations, lattice faulting/twinning and low-angle boundaries, are generated during growth of the films. A detailed view at the dislocation shows clearly bent lattice planes due to the additionally introduced lattice plane, as it is indicated by white lines in Figs 1c and d. The application of a higher negative substrate bias voltage leads to a higher kinetic energy of the deposited atoms and hence to an increasing number of defects in the films. An increasing density of dislocation-structure boundaries results in an increase of the orientation-difference of the adjacent crystals, breaking down the large column growth and thereby promoting a grain size (or column diameter) decrease.

Elemental maps were acquired using an energy dispersive x-ray spectrometer (EDS) attached to TEM in order to determine inhomogeneous distribution of alloying elements and/or precipitation of second phases through coating thickness. As can be observed in Figure 2, these maps showed that the composition is quite homogeneous along the thickness. Therefore, the different Ti-phases present in the coatings contain in solid solutions the same amount of Nb and Zr. Since maps depicted in Figure 2 are only qualitative, quantitative microanalysis were also performed from the spectra acquired during mapping. As is shown in Table 1, there are not significant variations in coating chemical composition related to increase the substrate bias voltage from 0 to -148 V, indicating that there is not a significant re-sputtering effect due to selective removal of ad-atoms by Ar ion-bombardment on growing film surface.

The selected area electron diffraction (SAED) patterns of Ti-Nb-Zr (wt. %) coatings are shown in the insets of 1a) and 1b) for a bias voltages values of -63 and -148 V, respectively. The ring character of the electron diffraction patterns indicates presence of nano-sized crystallites in both layers. Phase identification from the diffraction patterns is complicated by the fact that the samples might contain different phases with overlapping reflections (rings). Nevertheless, diffraction patterns of Fig. 1a and b show the presence of non-isotropic Debye rings filled by arced reflections, which correspond to the presence of a strong texture in the coatings. Although diffraction patterns of both layers are a priori quite similar, texture is somewhat more pronounced in the sample sputtered at -63 V. A detailed study of texture evolution in Ti-22Nb-10Zr (wt. %) coatings as a function of the bias voltage increase can be estimated from the extension of arcs from the superposition of single crystal (grain) spot pattern of the α” phase in [110] crystal zone axis simulated using the Jems software by Stadelmann [21] on the experimental ring pattern, as shown in the inset of Fig. 1a, corresponding to the sputtering coating deposited with a bias voltage value of -63 V. From this diffraction diagram it is evident that the crystal planes parallel to the substrate are $(002)_{\alpha''}$, with a deviation of ± 18º. The cubic β-phase shows even a stronger texture: $(110)_{\beta}$ with a deviation of ± 6º (inner arcs marked by arrows in the inset in Fig. 1a and indexed in the inset in Fig. 1b). In return, the rings distribution corresponding with diffraction pattern of the sputtering coating deposited with a bias voltage of -148 V (inset in Fig. 1b) is a bit different. This is indicative of changes in volume fractions of constituent phases and their crystal orientation. The inner ring of β phase shows six-fold symmetry typical for the [111] crystal zone axis (inset in Fig.1b). Rotating of this pattern ± 6° shows some of the arcs in the ring pattern. Preferential orientation of β phase grains parallel to the substrate is the crystal plane $(110)_{\beta}$, with a deviation of ± 6°, i.e. practically identical to the previous sample. On the other hand, the texture of the other two phases, i.e. hexagonal α and orthorhombic α”, is much weaker than in the sputtering deposition performed with a bias voltage of -63 V. The next intense rings in the inset of Fig. 1b, corresponding to $(101)_{\alpha}$ reflection and $(111)_{\alpha''}$ reflection, are continuous with nearly uniform intensity (nearly random texture); therefore we can conclude that the texture of these phases is weakened by increasing the bias voltage used.

Nano-diffraction phase and orientation maps were used to characterize the distribution of the different phases present in the coating, the variation of their grain sizes, as well as the evolution of their respective morphologies and textures as a function of the bias voltage increase. Figure 3a and c shows the phase maps of coatings deposited at -63 V watts and -148 V, respectively. In these figures, α, α'' and β- phases are colored in turquoise, purple and green, respectively, and points that no match with any of these phases are displayed as black. It can be seen in Fig 3a that the microstructure in the coating sputtered at -63 V consists of islands of α- and α”-Ti grains, with sizes ranging from 10 to 50 nm, embedded into a matrix of β-Ti with a grain size ranging from 50 to 200 nm. By contrast, these three phases appear alternating in a rather relatively regular manner in the coating sputtered at -148 V, as shown in Fig 3c. While the crystallites of α and β phases are mostly equiaxial, with grain sizes between 20 and 50 nm, the α“ martensite grains are columnar with aspect ratio up to 5:1 (Fig. 3c).

Figures 3b and d shows the orientation maps displayed in inverse pole figure (IPF) coloring schema for the same area analyzed in Figs 3a and c. Fig. 3b and d show for the β phase a very strong texture with {111} plane lying perpendicular to the substrate (almost all the green grains in Fig. 3 a and c present blue color in Fig. 3 c and d) while the orientation distribution α and α” martensite grains is more random. As {111} planes include <110> type directions, this result agrees with the texture previously observed in SAED patterns.

3.2 Crystallographic evolution

Figure 4 shows the evolution of the XDR patters as a function of the bias voltage used during the magnetron sputtering process. It can be observed that increasing the negative bias voltage from 0 to -148 volt leads to changes in the position, shape and intensity of diffraction peaks. None of the diffraction patterns obtained correspond to a pure Ti-phase, and they show a mix of three phases: α- (JCPDS card 044-1294), α’’- (JCPDS card 017-0102) and β-Ti (JCPDS card 044-1288). As the energy of the depositing ions depends on the bias voltage during the coating process, this parameter controls microstructural features such as balance between α, α’’ and β- phases within the coating, crystallite size, microstrain, and crystallographic texture. In fact, the evolution of asymmetric peak shape observed around of $2\theta = 38.24^0$, for sputtering deposition at 0 and -63 V, is a clear and unequivocal evidence that the phases concentration depends on bias voltage used, as observed in the TEM analysis referred to above.

The Rietveld analysis makes possible the decomposition of complex severely overlapped XRD patterns in terms of the diffraction patterns calculated from the crystal structures of present phases. Fig. 5 shows the contribution of α, α’’ and β- phases to the XRD patterns of Fig. 4 and Table 2 shows the mass fraction of these three phases. These results indicate that we can deposit coating with identical chemical composition but very different microstructural features, in terms of amount, morphology and crystallographic texture, as a function of bias voltage. This enables modeling the mechanical properties of a coating as a function of simple processing parameter.

Figure 6 shows the evolution of the three different phases present in the Ti-22Nb-10Zr (wt.%) coating as a function of the bias voltage used. As can be seen in Figure 6a, only the reflections (002), (012) and (013) of α-Ti are present in the sample sputtered at 0 bias voltage, indicating a strong {001} fiber texture. This texture was associated to a columnar structure that has grown with the dense plane (002) parallel to the substrate/coating interface. The progressive decrease of the intensity of the diffraction peaks observed in the samples sputtered at higher bias voltage and the emergence of the reflections of α-Ti was associated to weakening of the basal texture. As shown in Fig 6a, diffraction peaks of α-Ti have shifted to lower diffracting angles and get broader at the same time, indicating that a bias increase leads to an increase of residual stress state in the coatings, an increase of the defect density and a decrease of the crystallite size. Both the increase of defect density and the reduction of crystallite size contribute to the increase of the disorientation between adjacent crystallites separated by dislocation boundaries, which causes observed decrease in the {001} fiber texture.

As the bias voltage is increased, a progressive decrease of the intensity of the diffraction peaks of β-Ti was observed, associated to a decrease in the amount of this phase present within the coating. Figure 6b shows the change in the intensity in the case of the bias voltage equal to - 63 V, since the main fiber texture changes from (110) to (211). In return, for bias voltages higher than - 63 V, the intensity of (110) and (211) reflections is almost equal. This result was associated with a strong fiber texture with {110} and {211} plane lying parallel to the substrate. As {110} and {211} planes include <111> type directions, it agrees with the texture deduced from nano-diffraction orientation maps shown in Figs 3b and d. Assuming that at the early stage of deposition grains have a random orientation, those grains favored by the reduction in surface energy will grow faster at the expense of other grains. For bcc alloys, the (110) planes have the lowest surface energy and thus the {110} fiber texture is developed. However, considering the sputtering conditions used in this work, the compressive residual stress introduced on the coating is another parameter that has to be included in the total surface energy. The final film orientation is determined by minimization of the total surface energy, and this would explain also the presence of a {211} fiber texture on β-Ti. Fig 6b also shows the presence of the (002) reflection in the samples sputtered at a bias voltage higher than -98V, in agreement with the diffraction pattern shown in Fig 1b for the coating sputtered at -148V. Moreover, the growing widening of the β peaks, as the bias voltage increases, is an indication of large grains distortion; on the other hand, the growing intensity of α” peaks may be related to SIM transformation because of compressive residual stress. In fact, the higher the bias voltage value, the greater the intensity of (020) and (200) peaks are. This is a clear evidence of the SIM transformation, which is more and more pronounced for bias voltage higher than -63 V, since the $(020)_{\alpha''}$ reflection becomes stronger (Fig. 6b) while the $\{211\}_{\beta}$ reflection becomes weaker (Fig. 6c). Therefore, the higher the compression residual stresses magnitude, the higher the α” martensite percentage induced by SIM transformation (β → α”) and the lower the β phase content is. Table 2 shows the percentage evolution of these three phases and how the higher bias voltage values favor the formation of α” phase while the mass fraction of α-Ti remains rather constant. Furthermore, XRD patterns also reveal that classic Burgers orientation relationship, $\{001\}_{\alpha}//\{110\}_{\beta}$ and $[110]_{\alpha}//[111]_{\beta}$, is the majority between α and β phases and that the absence of $(111)_{\beta}$ and $(012)_{\beta}$ superlattice diffraction peaks suggest that the β phase is disordered. On the other hand, the strong presence of a $(111)_{\alpha''}$ texture arise from the {110} fiber texture of the β-phase as a consequence of well-known lattice correspondence between β-phase and α’’ martensite is: $[100]_{\alpha''}//[100]_{\beta}$, $[010]_{\alpha''}//[1\bar{1}0]_{\beta}$ and $[001]_{\alpha''}//[110]_{\beta}$.

3.3 Mechanical characterization

Substrate contributions to the hardness measurement of the coatings may be practically negligible in the case where the coatings are deposited on substrates with greater hardness value than the coating. However, if the plastic radius, R_p, and the maximum indentation depth, h_{max}, are comparable ($R_p/h_{max} \geq 1$). Then, the plastic volume, associated with a half sphere of radius R_p, is higher than the total layer thickness. It means that the substrate will introduce an elastic-plastic contribution to the hardness and Young’s modulus value. The R_p corresponding to the h_{max} values has been calculated [22]. As it can be seen from Figure 7, all the indentations generate a plastic radio, R_p, greater than the coating thickness, t, and therefore the substrate contribution that is exercised over the hardness and modulus measurements must be removed to evaluate real mechanical properties.

We can remove substrate contribution from the model developed by Iost et al. [23], which is based on an area law of mixture. Thereby, following the description in supplementary material it is possible to obtain the real hardness values from Eq. 10. Berkovich hardness evolution as a function of the load value increase with (full symbols) and without (open symbols) substrate influence are also shown in Figure 7. Here it is possible to see how hardness values, for load values higher than 1 mN, are practically constants for the remaining indentation depths. This is a clear evidence that the coating has a high homogeneity along the total layer thickness. Moreover, there is a big difference in the hardness values associated with the bias voltage. There is a great increase in the Berkovich hardness value when Ti-22Nb-10Zr (wt.%) coating is deposited with a bias voltage value of -63 V; the hardness then gradually decreases as the bias voltage is higher. This may be a priori surprising; typically; when the bias voltage increases, hardness values tend to follow the same trend due to increase in the magnitude of the residual compression stresses [24]. Opposite behavior observed in present study corroborates finding from XRD and TEM, where a higher α” martensite phase content with the increase of bias voltage was observed. Therefore, the decrease in the hardness values, as a function of bias, may be sign that the high compression stress magnitude can induce SIM transformation and therefore its magnitude would be reduced.

As it was mentioned above, the curvature of the coating can be used to measure qualitatively and quantitatively the type and magnitude of residual stresses in the coating.

Figure 8 shows the concave curvature corresponding to the Ti-22Nb-10Zr (wt.%) coating deposited with a bias voltage value of -63 V (a) and -148 V (b). From this figure is possible to see how the curvature radius decrease with the bias voltage increase. Thereby, curvature radius of silicon wafer coated with Ti-22Nb-10Zr (wt.%), R_0, deposited with a bias voltage of -63 and -148 V, is 14.51 and 101.56 m, respectively. From Stoney’s equation we can calculate the compressive residual stress $\sim$-700 MPa for bias -63 V and $\sim$ -100 MPa for bias -148 V. Such result is expected, since the magnitude of the compressive residual stresses decreases as a consequence of the induction of the martensitic transformation (β→α"). This decrease in the magnitude of the compressive residual stresses present has a direct impact on hardness values in the coating.

As with the Berkovich hardness values, the Young's modulus values are strongly influenced by the substrate, since ratio value between the plastic radio and layer thickness, R_p/t, is higher than 1 for all load used. Thereby, substrate exerts a strong influence, which is growing as the h_{max} increase regardless of the bias voltage values. As it can be seen in Figure 9, where Young's modulus value grow continuously. Thereby, the need to eliminate the substrate effect is evident in order to know the real Young's modulus value of the Ti-22Nb-10Zr (wt.%) coating as a function of bias voltage increase. For this object, the Doerner and Nix model [25] has been used, as we have done in previous works [26,27]. Figure 10 shows the real Young's modulus values of Ti-22Nb-10Zr (wt.%) coating as a function of bias voltage increase. Initially, the Young's modulus descends from 63 GPa, at a bias of 0 V, to 47 GPa, at -63 V and then progressively increases to 89 GPa at -148 V. These variations are associated to different β and α" martensite phases concentrations, since the α phase concentration practically remains constant for different bias voltages. Thus, the higher the concentration of α" martensite phase, the greater the real Young's modulus of Ti-22Nb-10Zr (wt.%) coating is. Therefore, it is evident that the contribution of α" martensite phase to Young's modulus is greater than that of β phase. Initial Young's modulus decrease, at -63 V, is associated with lower α phase concentration and above all with the change in the texture. Textures with larger lattice parameter produce lower Young's modulus value, as occurred in this case where the main $\{211\}_{\beta}$ fiber texture at -63 V shows larger lattice parameter in comparison with the main $\{110\}_{\beta}$ fiber texture at 0 V.

On the other hand, yield strength is modified because SIM transformation, which is typically induce after apply some external force, is grain size dependent [28]. Moreover, the presence of α and β phases with grain sizes around 50 nm is able to prevent the SIM transformation during cyclic load-bearing process, increasing the yield strength of this coating because of the elimination of the double yielding (its effects are discussed below). To shed light on the yield strength value increase when the bias voltage is increased, the yield strength is calculated through Tabor relationship ($H = 2.7 \cdot \sigma$) assuming that the coating shows a purely plastic behavior, i.e., the value of its hardening coefficient is 0. The evolution of $\sigma_{2.7}$ values as the bias voltages increase is shown in Table 3. The highest yield strength $\sigma_{2.7}$ value corresponds to bias voltage of -63 V as a direct consequence of the compressive residual stress introduction, which acts as a hardening component.

However, for higher bias voltages values, the $\sigma_{2.7}$ values decrease since the magnitude of residual compressive stresses drop due to higher SIM transformation induced during sputtering deposition.

Another point to take into account with regard to the applicability of this coating is related to the ductility. If the double yielding is eliminated in order to increase the yield strength of the coating, its ductility could be reduced and therefore its toughness will be lowered. A good way to characterize the higher or lower degree of ductility is through H/E ratio, which gives an idea of the toughness of the coatings. The dimensionless ratio H/E is a measure of the elastic strain and is strongly correlated with energy dissipation in the mechanical contact [29,30,31]. On the other hand, is also possible to calculate other similar ratio such as H^3/E^2, which is related to the higher or lower plastic deformation resistance [32]. The higher the plastic deformation resistance, the greater the ratio H^3/E^2 is. However, a high hardness alone is no guarantee of high toughness in highly loaded mechanical or tribological contact applications where fracture toughness and damage tolerance can be more critical. A reasonable way to increase this coefficient is to increase hardness values and reduce Young's modulus values. In fact, coatings with H/E ratio higher than 0.1 usually are considered tough and therefore it is possible to use this ratio in order to make a ranking of the coating toughness. Table 3 shows the H/E and H^3/E^2 ratios for the Ti-22Nb-10Zr (wt.%) coating as a function of bias voltage increase. The coating deposited at -63 V shows higher H/E and H^3/E^2 values, since it has the highest hardness and the lowest Young's modulus values, which is an optimum combination to achieve a high toughness and thus prolong lifetime of an implant coated with proposed coating.

3.4 Cell culture assays

As has been argued previously, the surface chemistry of different metallic alloys used for biomedical applications is directly related to the biocompatibility shown by these alloys. In this context, Ti-22Nb-10Zr (wt. %) composition must be analyzed in terms of its effect on cell adhesion, viability and proliferation, in order to reveal its future applicability as a coating in metallic substrates such as stainless steel 316 LVM or Ti6Al4V. For this purpose, MG-63 cells have been deposited on the surface of the cover glasses with and without sputtering coatings of pure Ti, Ti6Al4V and Ti-22Nb-10Zr (wt. %). The cellular viability has been assessed by the measurement of metabolic activity of cells after 1, 4 and 7 days of their cultivation (Fig. 11). Whereas the Ti-22Nb-10Zr coating behaves practically the same as pure titanium over the whole time course (Fig. 10a), there is approx. 1.75× higher metabolic activity of osteoblasts adhered to Ti-22Nb-10Zr coating compared to cells attached to Ti-6Al4V alloy (Fig. 10b). As time increase, Ti-22Nb-10Zr coating shows a similar trend to pure Ti and Ti6Al4V. Nevertheless, the applicability of Ti-22Nb-10Zr coating is well justified since it is free of toxic elements (Ni, Al and V) present in commercial stainless steel 316 LVM and Ti6Al4V. Moreover, this sputtering coating shows an exceptional mechanical properties, low Young's modulus and high Berkovich hardness values, which offer a better possibility for the design of a new implant generation that are long lasting and capable of promoting a direct bond between metallic surface and surrounding tissue bone.

4. Discussion

In the case of prosthesis material for artificial hip joints and knees, Young's modulus is only one of key parameters influencing stress shielding effect [33]. High fatigue resistance is also required, since the implants are subjected to cyclic loading under complicated stress conditions [28].This is doubtless one of the major problems related to the long-term safety of the material designed for biomedical applications. In this sense, the presence of a random α nano-grains distribution in Ti-22Nb-10Zr (wt.%) coating is necessary. Because its presence naturally increases the yield strength, since Young's modulus value for α phase is typically two times higher than β phase [34]. Thereby and thanks to the fact that the Nb content is below 39 wt%, α percentage remains practically constant, since it is almost independent of bias voltage increase. However, as the value of bias voltage increases from 0 to -148 V, the strong basal texture is broken in favor of a more random texture distribution, which may favor the reduction of the Young modulus value. Therefore, the evolution of the Young's modulus values showed by Ti-22Nb-10Zr (wt.%) have to be related to variations in the volume fraction ratio of β and α" phases as well as fiber texture evolution showed by XRD patterns. All these changes are directly related to the SIM (β→α") transformation, which is more pronounced as the bias voltage increases. However, its high increase can be a problem if SIM transformation take also places during those applications with high cyclic load-bearing; such transformation has been also related to a decrease in the fatigue resistance [35]. It is related to "double yielding" phenomenon, in which the first "yielding" corresponds to the critical stress to induce SIM transformation and the second yielding corresponds with the real elastic-plastic transition. Thus, if the first yielding value is too much low, coating may not be used in applications with high and cyclic load-bearing. Thereby, the presence of double yielding must be controlled and even mitigated. It is possible to achieve thanks to the control of the β grain sizes. If they are below 500 nm, SIM transformation is few favorable through external stresses as cyclic loads. Therefore the fatigue resistance of this nanostructure β rich coatings should not change. Nevertheless, as it was shown above, this SIM transformation can be activated, during sputtering deposition process, through bias voltage increase. Therefore, it possible to design from just one stoichiometric composition, coatings with different mechanical properties. A clear evidence of SIM occurrence as a consequence of bias voltage increase is shown in the α” peaks evolution (Fig. 6b), since peak intensities of $(110)_{\beta}$ and $(211)_{\beta}$ (Fig. 6c) are drastically reduced when, at the same time, the volume fraction of α” increases significantly. In fact, there is a great difference in the XRD α” patterns when the coating is produced with a bias voltages value higher than - 63 V. For 0 bias voltage value, there are only three main peaks: $(111)_{\alpha''}$, $(112)_{\alpha''}$ and $(220)_{\alpha''}$. The presence of the latter peak is related to higher Young's modulus value, as it has been shown by Matsumoto et al. in a similar β rich Ti alloy [36].This increase produces a high grain refinement and fiber texture evolution in a similar way to what happens in our case when bias voltage is increased. Considering the lattice correspondence between β and α” phases during SIM transformation in β rich Ti alloys: $<110>_{\beta}//[100]_{\alpha''}$, $<101>_{\beta}//[010]_{\alpha''}$ and $<110>_{\beta}//[001]_{\alpha''}$ [37,38], it is possible to explain the texture evolution showed by α” martensite phase. The fiber texture $(220)_{\alpha''}<001>_{\alpha''}$ is formed by obeying the lattice correspondence with $\{211\}_{\beta}<110>_{\beta}$ fiber texture. With increasing bias voltage, fiber texture of $\{200\}_{\beta}<110>_{\beta}$ and $(200)_{\alpha''}<001>_{\alpha''}$ are developed, suggesting that the development of $\{200\}_{\beta}<110>_{\beta}$ texture at bias voltage higher than -63 V is accompanied with the formation of $(200)_{\alpha''}[010]_{\alpha''}$ texture, holding the orientation relation between β and α”. Thereby, initial decrease in the Young's modulus value from 63 to 47 GPa is related to the disappearance of $(220)_{\alpha''}<001>_{\alpha''}$ texture and with the fact that $\{211\}_{\beta}<110>_{\beta}$ become the main texture when the bias voltage is increased from 0 to -63 V. For higher bias voltages, the magnitude of $(200)_{\alpha''}[010]_{\alpha''}$ texture become much bigger and therefore, it should reflect a continuous decrease in the Young's modulus values. However, the evidence of the values measured shows an opposite trend. This is related to fact that at bias voltages values higher than -63 V, the XRD patterns of α” martensite phase show the activation of different twinning systems such as $(111)_{\alpha''}\langle 110\rangle_{\alpha''}$ and $(110)_{\alpha''}\langle 110\rangle_{\alpha''}$ as a consequence of SIM transformation. The presence of this twinning systems without doubt increases the Young’s modulus values.

On the other hand, the reduction of the Young's modulus is not enough to guarantee a direct bond between the bone tissue and the surface of the metal implant, thus achieving full osseo-integration of the implant. Therefore, the second major challenge to be solved is the lack of osseo-integration of the current metal alloys (TI6Al4V, AISI 316 LVM, CoCrMo), since the implants are usually encapsulated by non-adherent fibrous tissue [39]. The thickness of this tissue, which is a mechanism of protection of the human body, depends on the interfacial movement and, therefore, on how well anchored the implant is. In fact, the greater the mismatch, the greater the thickness of this capsule being able to reach thicknesses of up to hundreds of microns. The presence of this tissue results in increased corrosion and therefore increasing release of toxic ions and debris that accelerates wear and, in the long term, the implant loosens, which can produce bone fracture in the region adjacent to the implant. Therefore, from bioactivity point of view, surface modification should be aimed at increasing the osseo-integration in order to minimize the presence of this fibrous tissue. In this sense, Ti-22Nb-10Zr (wt.%) coating has shown at least the same biocompatibility in comparison with pure titanium. More importantly, Ti-22Nb-10Zr coating enables much better adhesion of osteoblasts to the surface when compared to Ti6Al4V. Metabolic activity of Ti-22Nb-10Zr increases only after 24 hours of culture which reflects cell adhesion rather than cell proliferation. This is undoubtedly a clear indication that this coating would present a better and more direct bond with the surrounding bone tissue than the Ti6Al4V.

5. Conclusion

We have shown bottom-up design of non-toxic β-rich Ti-22Nb-10Zr (wt.%) coatings with very different microstructural features, in terms of balance between α, α” and β-phase and morphology and crystallographic texture of these phases. All these structural changes can be controlled by single deposition parameter: bias voltage. Increase in bias induces SIM transformation during sputtering deposition. β→α” transformation modifies the mechanical properties as a function of β/α” ratio. Since while the mass fraction of α-Ti remains rather constant, α” phase forms at the expense of the β-phase as negative bias voltage is increased. Furthermore, the bias increase leads also to an increasing number of defects in the sputtered alloy and to a lower crystallite size, resulting in a higher disorientation between adjacent crystallites separated by interphase boundaries. Such randomization of the microstructure causes a transition from a columnar to a finer and more equiaxed grain structure and a weakening of the crystallographic texture of the α, α” and β-phases.

All these changes have a direct impact in the mechanical properties such as hardness and Young’s modulus values. The coating sputtered with bias voltage of -63V is of special interest for biomedical applications, since it shows low Young´s modulus of 47 GPa which is quite close to human bone (~ 30 GPa) together with high Berkovich hardness of 5.6 GPa and bioactivity almost double compared to Ti6Al4V alloy.

Acknowledgements

The authors wish to express their thanks for the financial support of the Czech Science Foundation through the project 14-32801P. Nano-characterization was carried out on equipment funded by EPSRC through EP/K005103/1 project. We are also grateful to CENIM’s X ray laboratory for the support given on the analysis of XRD patterns. M.K. would like to acknowledge financial support of the ERDF in the frame of the project No. CZ.02.1.01/0.0/0.0/15_003/0000485.

References

---

[1] R. Banerjee, S. Nag, H.L. Fraser. Mater. Sci. Eng. C. 25 (2005) 282.

[2] B. Gasser. Design and engineering criteria for titanium devices. In: brunette, D.M., Tengvall, P., Texfor, M., Thomsen, P. (Eds.), Titanium in Medicine. Springer, New York, pp. 673-701.

[3] Y.L. Zhou, M. Niinomi. Mater. Sci Eng. C. 29 (2002) 314.

[4] J.-Y. Rho, T.Y. Tsui, G.M. Pharr. Biomaterials. 18 (1997) 1325.

[5] M. Niinomi. Mater. Sci. Eng. A. 243 (1998) 231.

[6] R.B. Osman, M.V. Swain. Materials. 8 (2015) 932.

[7] M. Geetha, A.K. Singh, R. Asokamani, A.K. Gogia. Prog. Mater. Sci 54 (2009) 397.

[8] S. Ozan, J. Lin, Y. Li, R. Ipek, C. Wen. Acta Biomater. 20 (2015) 176.

[9] M.T. Mohammed, Z.A. Khan, M. Geetha, A.N. Siddiquee. J. Alloy. Comp. 634 (2015) 272.

[10] X. Zhao, M. Niinomi, M. Nakai. J. Mech. Behav. Biomed. Mater. 4 (2011) 2009.

[11] Y.L. Hao, S.J. Li, S.Y. Sun, R. Yang. Mater. Sci. Eng. A. 441 (2006) 112.

[12] J.I. Kim, H.Y. Kim, T. Inamura, H. Hosoda, S. Miyazaki. Mater. Sci. Eng. A. 403 (2005) 334.

---

[13] H.Y. Kim, Y. Ikehara, J.I. Kim, H. Hosoda, S. Miyazaki. Acta Mater. 54 (2006) 2419.

[14] H. Matsumoto, S. Watanabe, S. Handa. Mater. Trans. 46 (2005) 1070.

[15] S.J. Li, M. Niinomi, T. Akahori, T. Kasuga, R. Yang, Y.L. Hao. Biomaterials. 25 (2004) 3369.

[16] E. Eisenbarth, D. Velten, M. Miler, R. Thull, J. Breme. Biomaterials. 25(26) (2004) 5705.

[17] M. Abdel-Hady, H. Fuwa, K. Hinoshita, H. Kimura, Y. Shinzato, M. Morinaga. Scripta Mater. 57 (2007) 1000.

[18] Pearson's Crystal Structure Database for Inorganic Compounds, Release 2016/2017. Materials Park: ASM International, 2016.

[19] W.C. Oliver, G.M. Pharr, J. Mater. Res. 7 (1992) 1564.

[20] G.C. Stoney. Proc. R. Soc. Lond. A 82 (1909) 172.

[21] Stadelmann P., Available from: http://www.jems-saas.ch

[22] E. Frutos, M. Callisti, M. Karlik, T. Polcar. Mater. Sci. Eng. A. 632 (2015) 137.

[23] K. Rahmoun, A. Iost, V. Keryvin, G. Guillemont, N.E. Chabane Sari. Thin Solid Films. 518 (2009) 213.

[24] S. Achache, S. Lamri, A. Alhussein, A. Billard, M. Francois, F. Sanchette. Mater. Sci. Eng. A. 673 (2016) 492.

[25] M.F. Doerner, W.D. Nix, J. Mater. Res. 1 (1986) 601.

[26] E. Frutos, J.L. González-Carrasco, N. Vilaboa, R. Martínez-Morillas. Intermetallics. 19 (2011) 260.

[27] E. Frutos, J.L. González-Carrasco, T. Polcar. J. Mech. Behav. Biomed. 57 (2016) 310.

[28] Y.L. Hao, M. Niinomi, D. Kuroda, K. Fukunaga, Y.L. Zhou, R. Yang, A. Suzui. Metall Trans A. 33 (2002) 3137.

[29] V. Ivashchenko, S. Veprek, A. Pogrebnjak, B. Postolnyi. Sci. Technol. Adv. Mater., 15 (2014) 25007.

[30] E. Frutos, A. Cuevas, J.L. González-Carrasco, F.Martín. J. Mech. Behav. Biomed. 16 (2012) 1.

[31] E. Frutos, J.L. González-Carrasco. J. Mech. Behav. Biomed. 46 (2015) 93.

[32] T.Y. Tsui, G.M. Pharr, W.C. Oliver, et. al. Mater .Res. Soc. Symp. Proc. 383 (1995) 447.

[33] M. Niinomi. Metall. Mater. Trans A. 33 (2002) 477.

[34] Z. Fan. Scripta Metall. Mater. 29 (1993) 1427.

[35] E.W. Collings, H.L. Gegel. Scripta Metall. 7 (1973) 437.

[36] H. Matsumoto, S. Watanabe, S. Hanada. Mater. Trans. 46 (2005) 1070.

[37] T.W. Duering, J. Albrecht, D. Richter, P. Fisher. Acta Metall. 30 (1982) 2161.

[38] H. Sasano, T. Suzuki, O. Nakano, H. Kimura. Titanium ’80, Science and Technology AIME, 1980, p. 717.

[39] J.M. Anderson, A. Rodriguez, D.T. Chang. Semin Immunol. 20(2) (2008) 86.

Figure captions

Figure 1. TEM micrographs of Ti-Nb-Zr sputtering coatings on Si substrate: (a) diffraction contrast of the coating deposited with a bias of -63 V, the inset shows corresponding SAED pattern with superposed simulated single crystal pattern in [1,1,0] zone axis of the orthorhombic α” phase; the arcs of cubic β-phase reflections are indicated

by red arrows; (c) bias voltage of -63 V, atomic resolution micrograph, white line indicates bent atomic planes; (b) diffraction contrast of the coating deposited with a bias of -148 V, the inset shows corresponding SAED pattern with superposed simulated single crystal pattern in [1,1,1] zone axis of the cubic β phase; (d) bias voltage -148 V, atomic resolution micrograph, white line indicate an edge dislocation and bent atomic planes.

Figure 2. STEM-HAADF micrograph of the sputtering coating deposited on Si substrate with a bias voltage of -63 Volts and corresponding energy dispersive spectroscopy (EDS) maps of Ti, Nb, and Zr.

Figure 3. TEM nanodiffraction phase imaging and orientation maps of Ti-Nb-Zr sputtering coatings: (a) (b) bias voltage of -63 V, (c) (d) bias voltage of -143 V. The identified phases are denoted by turquoise (hexagonal α phase), green (cubic β-phase) and purple (orthorhombic α" phase) colors, points with no match are displayed as black. Orientation maps are colored according to inverse pole figures in the bottom part of the figure corresponding to *z* axis (electron incidence) and the phases present.

Figure 4. X-Ray diffractions patterns as a function of the increasing bias voltage for Ti-22Nb-10Zr (wt.%) sputtering coating.

Figure 5. Deconvolution of X-Ray patterns for two bias voltage conditions. a) Ti-22Nb-10Zr (wt.%) coating deposited with a -63 bias voltage value and b) with a -148 bias voltage value. In both cases, letters code means: O corresponds to the original X-Ray pattern, C is the total convolution of different phases present in the coating, D is the difference between the original and the total convolution pattern, α" corresponds with the orthorhombic martensite phase, β is the body-centered cubic (BCC) phase and α is the hexagonal closed-packed (HCP) phase.

Figure 6. Evolution of the phases present in the Ti-22Nb-10Zr (wt.%) coating as a function of the increasing bias voltage: (a) hexagonal close-packed α phase, (b) orhorombic α" phase, (c) body-centered cubic β phase.

Figure 7. Influence of the bias voltage on the Berkovich hardness evolution as a function of the plastic ratio, R_p, associated with the maximum indented depth, h_{max}, and the total thickness, *t*, of the coating.

Figure 8. The concave curvature corresponding to the Ti-22Nb-10Zr (wt.%) coating is shown for bias voltage value of -63 V (a) and -148 V (b). As the bias voltage increase, the curvature radius, R, decrease.

Figure 9. Influence of the Young's modulus evolution as a function of the bias voltage and as a function of the plastic radio, R_p, associated with the maximum indented depth, h_{max}, and the total thickness, t, of the coating ratio.

Figure 10. Real Young's modulus values of Ti-22Nb-10Zr (wt.%) coating as a function of bias voltage increase and how this value change as a function of the phases percentages present in the coating.

Figure 11. The compatibility of human osteoblasts with Ti-22Nb-10Zr coating, compared with pure titanium (a) and Ti6Al4V (b).

Table 1. Chemical compositions of the sputtering coatings deposited at -63 and -148 bias voltage values.

Table 2. Evolution of the phase composition with bias voltage.

Table 3. Evolution, as a function of bias voltages increase, of Young's reduced and real Young's modulus, E_{fr} and E_f, respectively, Berkovich hardness, H, and Yield strength, $\sigma_{2.7}$.

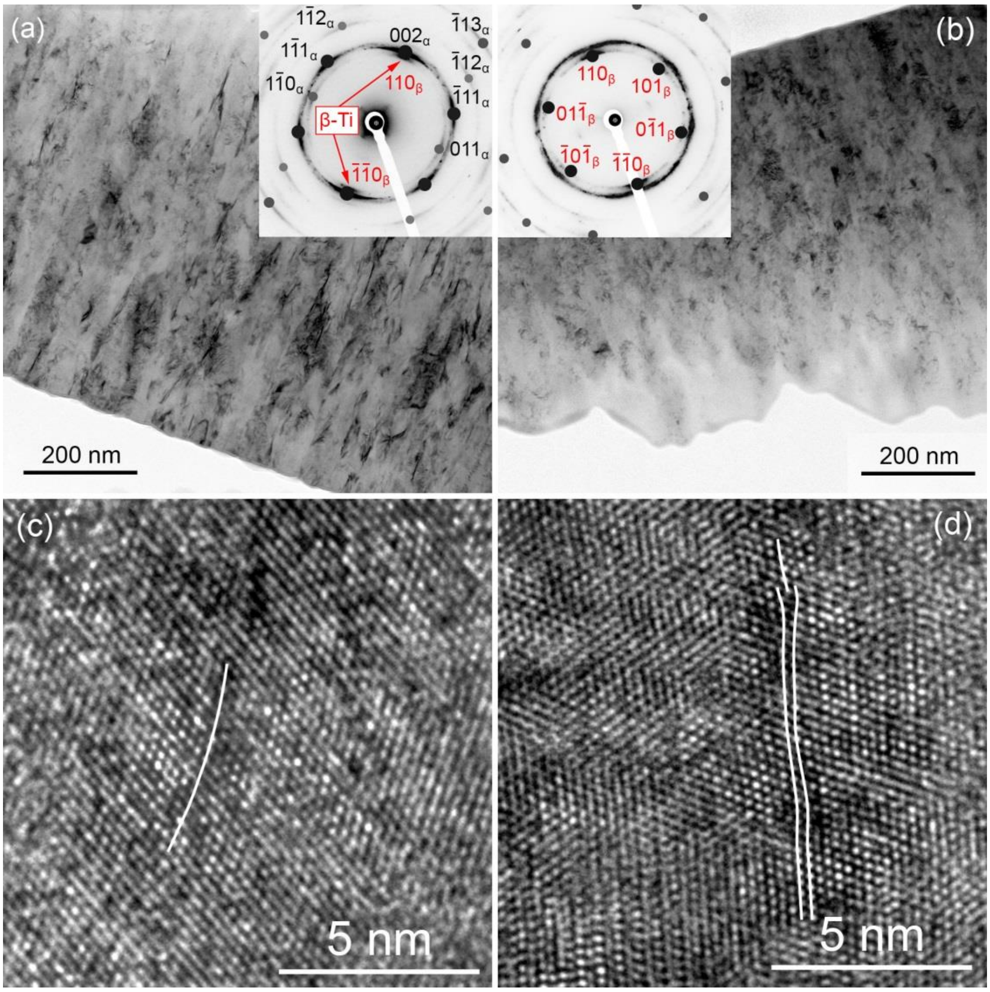

Figure 1. TEM micrographs of Ti-Nb-Zr sputtering coatings on Si substrate: (a) diffraction contrast of the coating deposited with a bias of -63 V, the inset shows corresponding SAED pattern with superposed simulated single crystal pattern in [1,1,0] zone axis of the orthorhombic α" phase; the arcs of cubic β-phase reflections are indicated by red arrows; (b) diffraction contrast of the coating deposited with a bias of -148 V, the inset shows corresponding SAED pattern with superposed simulated single crystal pattern in [1,1,1] zone axis of the cubic β phase; (c) bias voltage of -63 V, atomic resolution

micrograph, white line indicates bent atomic planes; (d) bias voltage -148 V, atomic resolution micrograph, white line indicate an edge dislocation and bent atomic planes.

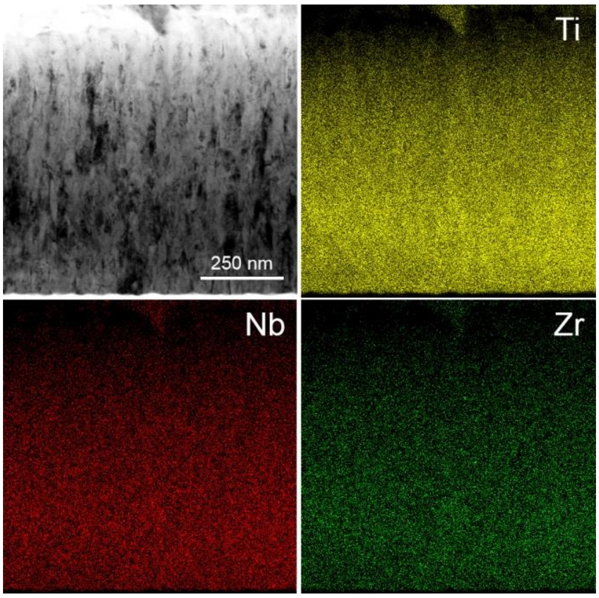

Figure 2. STEM-HAADF micrograph of the sputtering coating deposited on Si substrate with a bias voltage of -63 Volts and corresponding energy dispersive spectroscopy (EDS) maps of Ti, Nb, and Zr.

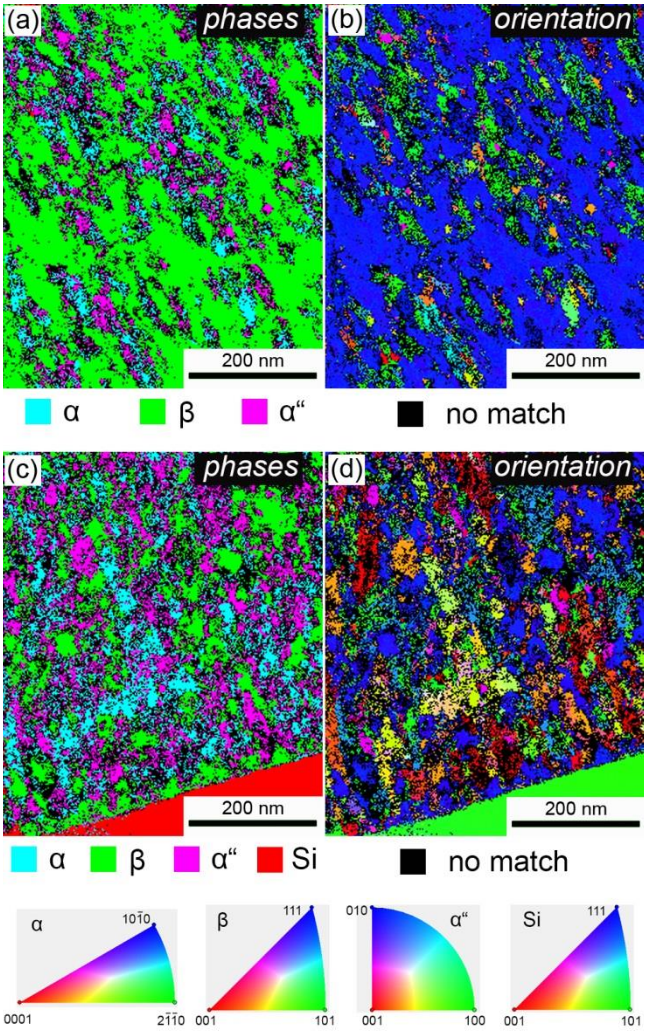

Figure 3. TEM nanodiffraction phase imaging and orientation maps of Ti-Nb-Zr sputtering coatings: (a) (b) bias voltage of -63 V, (c) (d) bias voltage of -143 V. The identified phases are denoted by turquoise (hexagonal α phase), green (cubic β-phase) and purple (orthorhombic α” phase) colors, points with no match are displayed as black. Orientation maps are colored according to inverse pole figures in the bottom part of the figure corresponding to *z* axis (electron incidence) and the phases present.

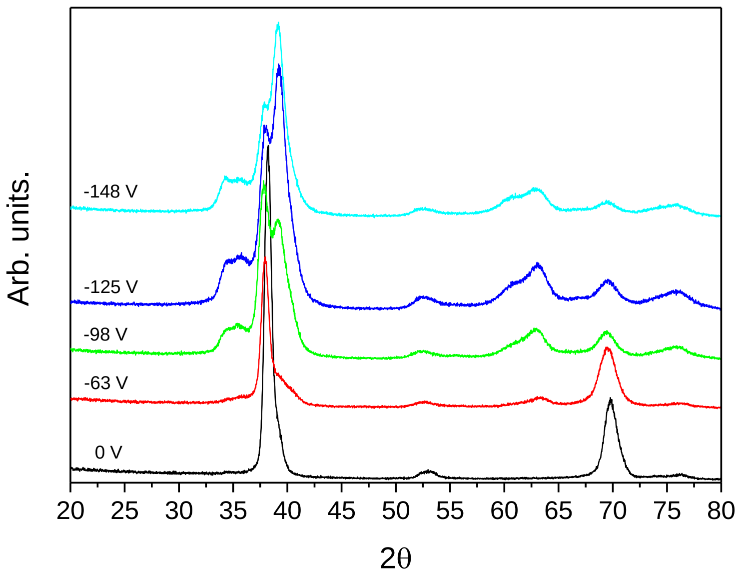

Figure 4. X-Ray diffractions patterns as a function of the increasing bias voltage for Ti-22Nb-10Zr (wt.%) sputtering coating.

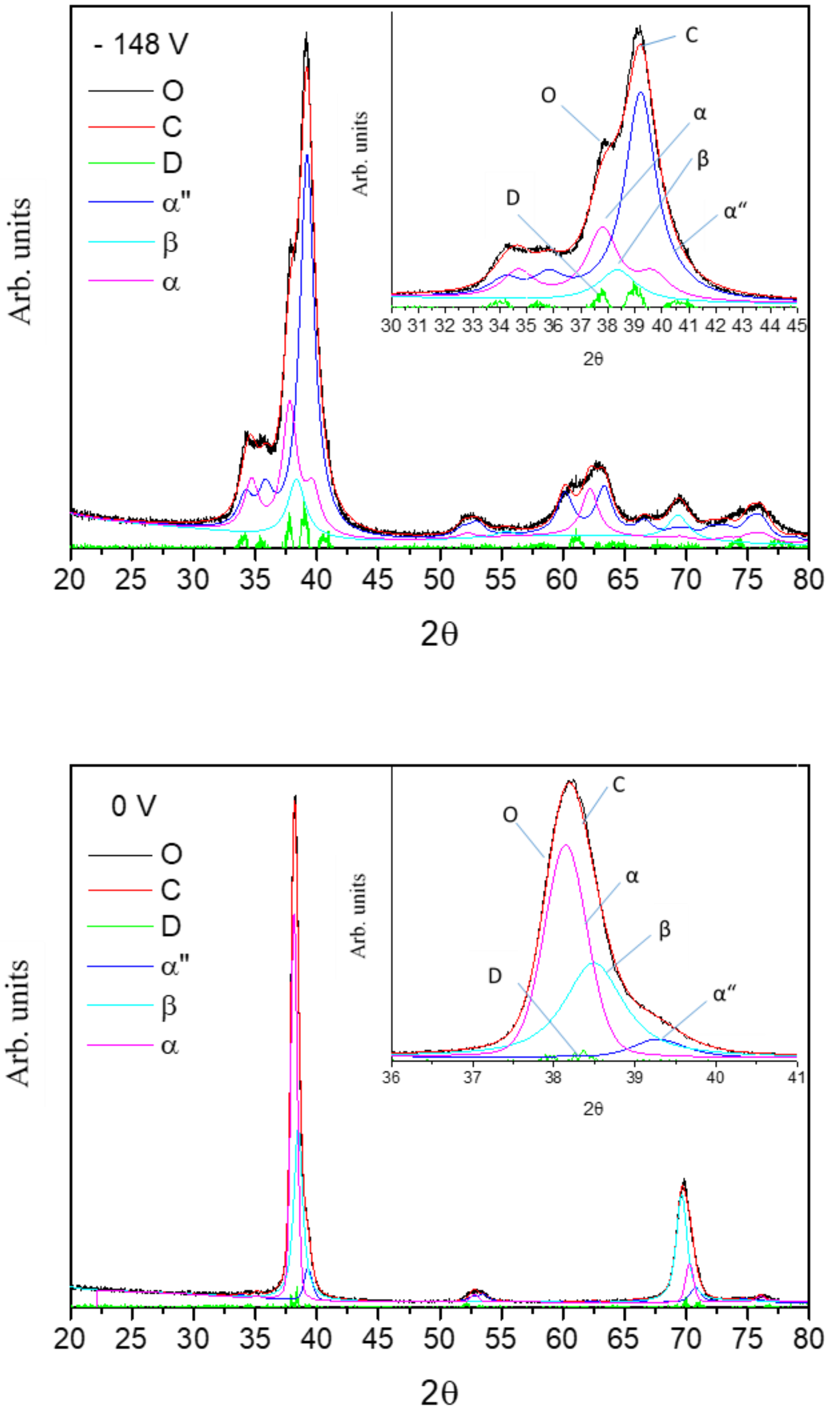

Figure 5. Deconvolution of X-Ray patterns for two bias voltage conditions. a) Ti-22Nb-10Zr (wt.%) coating deposited with a -63 bias voltage value and b) with a -148 bias voltage value. In both cases, letters code means: O corresponds to the original X-Ray pattern, C is the total convolution of different phases present in the coating, D is the difference between the original and the total convolution pattern, α" corresponds with the

orthorhombic martensite phase, β is the body-centred cubic (bcc) phase and α is the hexagonal closed-packed (hcp) phase.

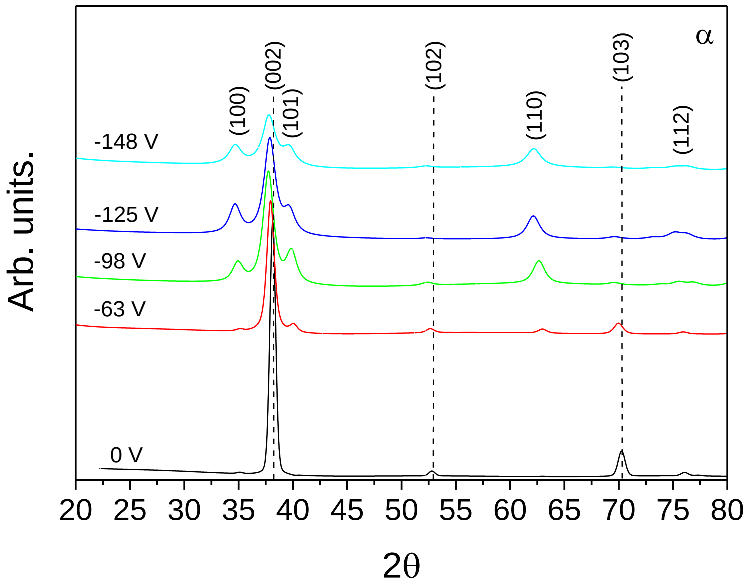

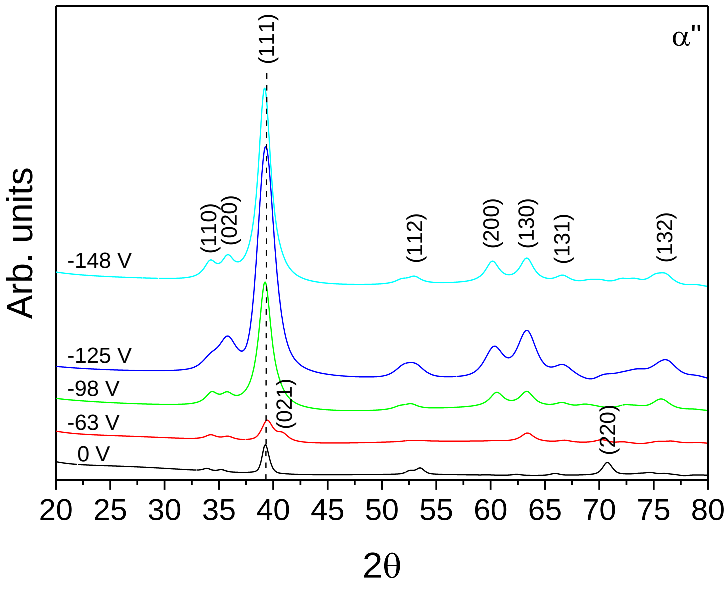

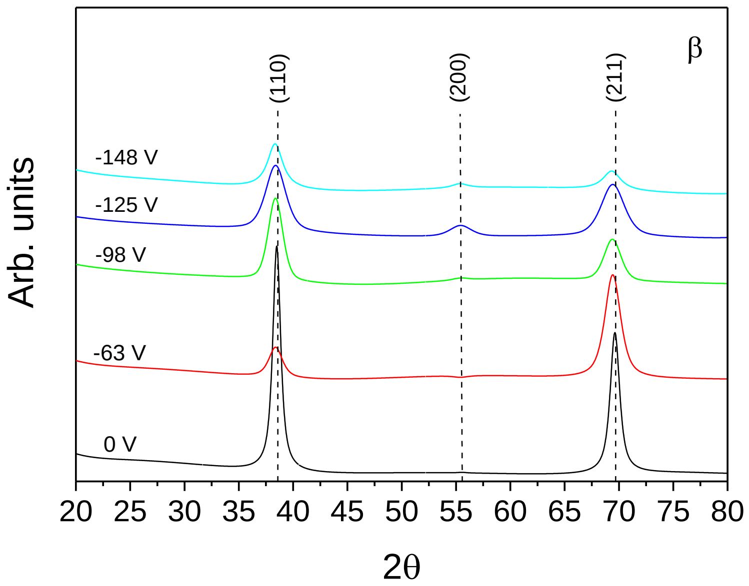

Figure 6. Evolution of the phases present in the Ti-22Nb-10Zr (wt.%) coating as a function of the increasing bias voltage: (a) hexagonal close-packed α phase, (b) orhorombic α” phase, (c) body centered cubic β phase.

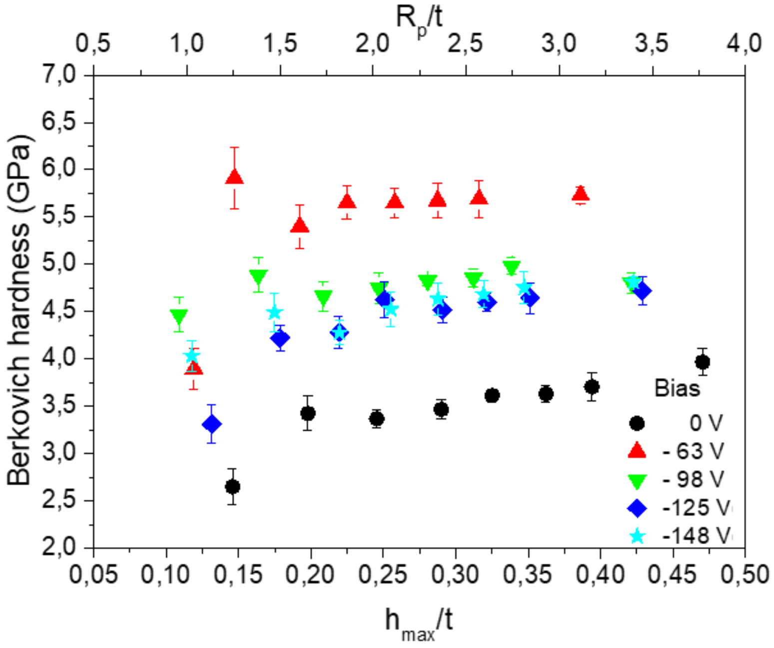

Figure 7. Influence of the bias voltage on the Berkovich hardness evolution as a function of the plastic ratio, R_p, associated with the maximum indented depth, h_{max}, and the total thickness, *t*, of the coating.

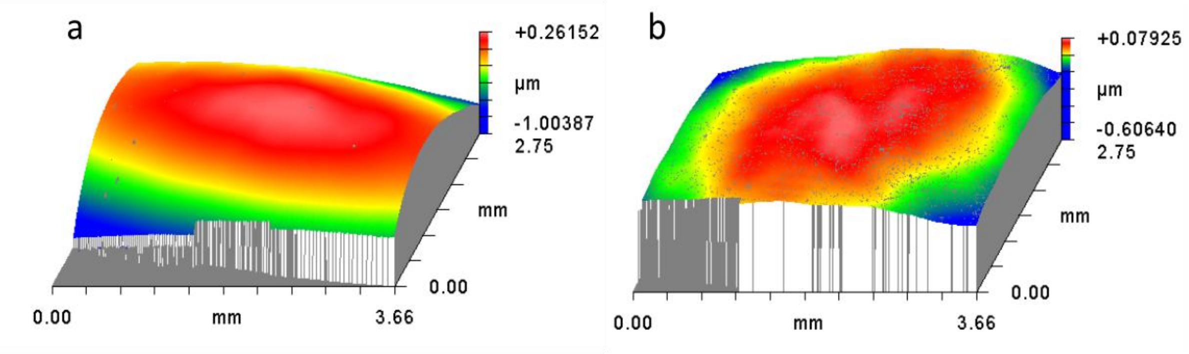

Figure 8. The concave curvature corresponding to the Ti-22Nb-10Zr (wt.%) coating is shown for bias voltage value of -63 V (a) and -148 V (b). As the bias voltage increase, the curvature radius, R, decrease.

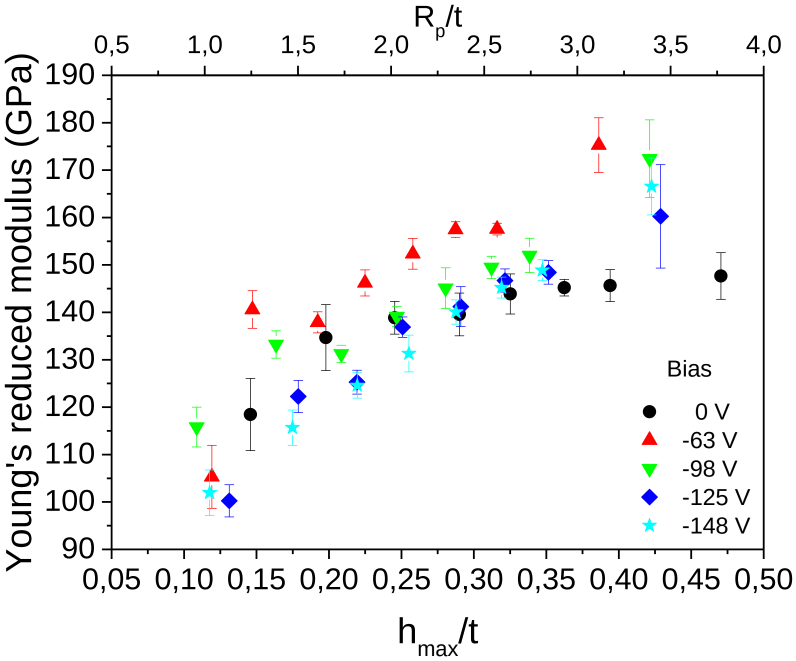

Figure 9. Influence of the Young's modulus evolution as a function of the bias voltage and as a function of the plastic radio, R_p, associated with the maximum indented depth, h_{max}, and the total thickness, t, of the coating ratio.

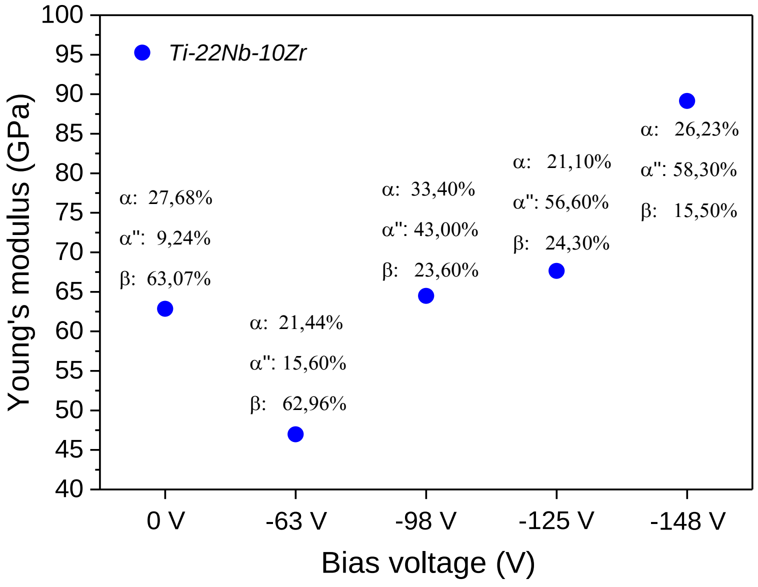

Figure 10. Real Young's modulus values of Ti-22Nb-10Zr (wt.%) coating as a function of bias voltage increase and how this value change as a function of the phases percentages present in the coating.

Figure 11. The compatibility of human osteoblasts with Ti-22Nb-10Zr coating, compared with pure titanium (a) and Ti6Al4V (b).

Ti-Nb-Zr	**at. %**			**wt. %**		
	Ti	*Nb*	*Zr*	*Ti*	*Nb*	*Zr*
-63 V	80,17	13,58	6,25	67,69	22,26	10,05
-148 V	79,83	13,32	6,86	67,23	21,77	11,01

Table 1. Chemical compositions of the sputtering coatings deposited at -63 and -148 bias voltage values.

Ti-22Nb-10Zr (wt.%)	*α phase (%)*	*α'' phase (%)*	*β phase (%)*
0 V	27,68	9,24	63,07
-63 V	21,44	15,60	62,96
-98V	33,40	43,00	23,60
-125 V	21,10	54,60	24,30
-148 V	26,23	58,30	15,50

Table 2. Evolution of the phase composition with bias voltage.

Ti-22Nb-10Zr (wt.%)	E_{fr} *(GPa)*	E_f *(GPa)*	*H (GPa)*	H/E_f	H^3/E_f^2 *(GPa)*	$\sigma_{2.7}$ *(GPa)*
0 V	66	63	2.9	0.047	0.006	1.1
-63 V	50	47	5.6	0.120	0.081	2.1
-98V	68	64	4.7	0.072	0.024	1.7
-125 V	71	68	4.2	0.063	0.017	1.6
-148 V	93	89	4.4	0.055	0.011	1.6

Table 3. Evolution, as a function of bias voltages increase, of Young's reduced and real Young's modulus, E_{fr} and E_f, respectively, Berkovich hardness, H, and Yield strength, $\sigma_{2.7}$.